Aerospace Science and Technology 84 (2019) 530–542

Contents lists available at ScienceDirect

Aerospace Science and Technology

www.elsevier.com/locate/aescte

Parametric study of a VLS based on 2-D FSI analysis

HyunShig Joo [a], Haeseong Cho [b], Younghun Lee [a], SangJoon Shin [c,*], Jack J. Yoh [c], Jae-Cheol Shin [d]

[a] Department of Mechanical and Aerospace Engineering, Seoul National University, 1 Gwanak-ro, Gwanak-gu, Seoul 151-744, Republic of Korea
[b] BK21 Plus Transformative Training Program for Creative Mechanical and Aerospace Engineers, Institute of Advanced Machines and Design, Seoul National University, 1 Gwanak-ro, Gwanak-gu, Seoul 151-744, Republic of Korea
[c] Department of Mechanical and Aerospace Engineering, Institute of Advanced Aerospace Technology, Seoul National University, 1 Gwanak-ro, Gwanak-gu, Seoul 151-744, Republic of Korea
[d] Agency for Defense Development, Yuseong, Daejeon 305-600, Republic of Korea

ARTICLE INFO

Article history:
Received 28 May 2018
Received in revised form 16 August 2018
Accepted 29 October 2018
Available online 6 November 2018

Keywords:
Vertical launching system
2D fluid–structure interaction
Elastoplasticity
Contact analysis
Level-set method
Parametric study

ABSTRACT

Vertical launching system (VLS) is useful in operating and sheltering high-speed rockets. The aft closure in the plenum plays a significant role in protecting the interiors from the exhaust gas induced by the ignition of adjacent or in-positioned canisters. During the aft opening/closing event, a complex flow is propagated into the VLS. By presence of such structural components, it is necessary to analyze the interaction between the deforming aft closure and a highly pressurized plume.

This paper presents a two-dimensional fluid–structure interaction (FSI) simulation under high pressure loading condition for preliminary design of VLS. A quadrilateral 9-node element based on co-rotational (CR) framework is used to predict the geometrically/materially nonlinear deformation of the aft closure while supersonic impinging jet plume is predicted by fully Eulerian modeling. A contact mechanism is also utilized to apply reaction forces between the structures and inclined plenum using a penalty term. The interface and boundary conditions are obtained by the hybrid particle level-set method via the Ghost framework. Furthermore, a parametric study is conducted by changing the thickness of the aft closure and the inclined angle of the plenum. It is expected that the magnitudes of pressure and temperature can be decreased by the introduction of appropriate thickness of the aft closure and inclined angle in the plenum.

1. Introduction

A VLS is a representative system that provides pre-launch and launch sequencing. In ship environments, six to forty vehicles are stored in VLS and sequentially launched. Extant studies conducted experiments [1–4] on the jet and its configuration for a few decades. Gummer [1] revealed that the impingement of a supersonic jet on a solid surface is a complex phenomenon in terms of a uniform and axisymmetric analysis. Static pressures measured from jet impingement are influenced by the distance from the normal surface in [2,3,5]. A wide variety of flow patterns are observed in [3] by using three different wedges arranged in the jets. Boundary layer separation is also observed by a clear area in the surface flow induced by a bow shape first shock reflection upstream. Masuda and Moriyama [6] experimentally and numerically investigated an the under-expanded coaxial jet and indicated that the shock structure in the jet is strongly dependent on both ejection angle of the nozzle and the pressure ratio of jet condition. Acoustic and unsteady surface pressure measurements confirmed that the stagnation bubble is formed due to the impingement of the shear layer slip line in [7].

In a similar fashion, several studies [8] focused on illuminating the highly complex flows in jet plume. Based on the impingement of inviscid axisymmetric jets, Rubel [8] presented three distinct classes of behavior in which the appearance of stagnation bubbles are dependent on the defect regime. With respect to a three-dimensional structure, Kim and Chang [9] characterized the flow field with several discontinuities such as barrel shock, exhaust gas jet boundary, Mach disk, reflected shock, plate shock, and a stagnation bubble affected by inclined plates. For the use of various types of rockets, a preliminary design of a VLS was attempted in [10]. Bertin [11] indicated the complications in the generated jet flow due to the presence of the grid diffuser, converging section and

* Corresponding author.
E-mail addresses: joohyunshig@snu.ac.kr (H. Joo), nicejjo@snu.ac.kr (H. Cho), acd1236@snu.ac.kr (Y. Lee), ssjoon@snu.ac.kr (S. Shin), jjyoh@snu.ac.kr (J.J. Yoh), jcshin@add.re.kr (J.-C. Shin).

https://doi.org/10.1016/j.ast.2018.10.038
1270-9638/

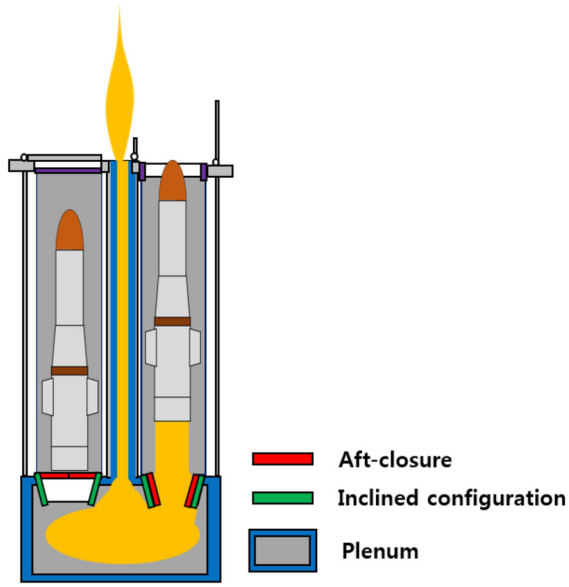

Fig. 1. Scheme of typical VLS. (For interpretation of the colors in the figure(s), the reader is referred to the web version of this article.)

other components from experimental results. Recently, Lee et al. [12–15] presented numerical solutions for a jet impingement flow in a VLS type internal missile launcher.

However, the effect of the structures requires further investigation to understand the aforementioned complex flow behavior and to predict an increasingly realistic and efficient design of a ducted plume system. A typical VLS scheme is shown in Fig. 1. First, it is necessary to completely open an aft closure by the initial ignition of rocket to guide the highly pressurized plume into the uptake duct. Additionally, it is required to be completely closed to protect the interiors from the rocket plume launched by the neighboring canisters. Second, the complex flow propagation may vary with respect to the specific angle of the gas gathering tank (GGT) inside the rocket system. In reality, the aft closure exhibits an elasto-plastic behavior due to exposure to high pressure and temperature from the jet impinging plume and is bounced out from an inclined plate to propagate impinging jet plume into the VLS.

In the current study, two key factors, namely the aft closure and the angle of inclined structures in GGT, are considered to reveal and further design a highly efficient VLS. Although a VLS is fully three dimensional and viscosity influences the flow field in GGT, it entails significant computational requirements for FSI analysis including the parametric studies. Instead, the objectives of the present numerical simulation involve understanding various phenomena of the propagated pressure and temperature in a VLS by changing two factors. Also, the efficiency of analysis should be considered to relieve the computational cost incurred. Hence, a two-dimensional FSI analysis established to simulate the event of two hang fire cases. Based on the CR formulation, non-linear structural model using 9-node planar element is used to estimate large deflection in aft closure. Elasto-plastic behavior and contact mechanism are included to consider the large and reflected deflection from the inclined structures in GGT. Such structural model is tightly coupled with jet impinging plenum in the full Eulerian modeling. A hybrid particle level set method is used based on the immersed boundary condition to exchange plume load and deflection of structures. A zero value in level set defines the boundary between structures and flow field. By using the tightly coupled Lagrangian–Eulerian method, flow and structures are independently predicted and exchange aerodynamics (total pressure) and geometry (displacement) at each time step. The novelty of the present approach is the absence of the necessity to regenerate grids during FSI simulations. In the validation procedure of the present simulations, each fluid/structural and coupled problem is compared with a commercial software (ANSYS and ABAQUS). Finally, the estimated pressure and temperature in a complex flow field exhibit a trend with respect to the thickness of the aft closure and inclination angle of the inclined structures in GGT.

2. Numerical methodology

In this section, numerical strategies are described in detail. First, the CR formulation is utilized for the structural analysis by separating geometrical and material nonlinearity. In the flow field, a two-dimensional compressible gas dynamic equation is defined by using plume gas composition based on ammonium perchlorate (AP). Subsequently, the tightly coupled FSI approach is utilized to track the interface and boundary conditions via the level-set method.

2.1. Governing equation for the structural analysis

2.1.1. Co-rotational formulation

Based on the assumptions of small strain and large displacement, the CR formulation is used to predict an accurate geometrically nonlinear structural analysis. The main advantage of the CR formulation is that each geometrical and material nonlinearity is artificially separated. Rankin and Brogan [16] suggested that element-independent co-rotational (EICR) description is obtained by using the existing finite element method. Battini [17] developed a nonlinear co-rotational 4-node plane element without the assumptions to derive linear elements. Previous studies [18, 19] also suggested a consistent CR formulation for time-transient analysis with a higher order solid-like planar element and a triangular/quadrilateral planar element including in-plane rotational degree-of-freedom (DOF).

In the CR formulation, deformed configuration is estimated by using three rotations based on three different coordinates. The rigid-body ($\underline{\underline{R}}_r$), global ($\underline{\underline{R}}_g$), and local rotation ($\underline{\underline{R}}_l$) are shown in Fig. 2. The rigid-body rotation of the 9-node planar element is defined by the translation of global nodal points as follows:

$$\underline{u}_d^k = \left\{ \underline{u}_o^k + \underline{u}_g^k - \underline{u}_c^k - \underline{u}_{g,c}^k \right\} \tag{1a}$$

$$\tan\theta_r = \frac{\sum_{k=1}^{9} u_{g,x}^k u_{d,y}^k - u_{g,y}^k - u_{d,1}^k}{\sum_{k=1}^{9} u_{g,y}^k u_{d,y}^k + u_{g,1}^k u_{d,x}^k} \tag{1b}$$

Details of the present kinematics are explained in [17,19]. The displacement vectors of the local and global coordinates are defined as follows:

$$\underline{u}_l = \{u_l^1, v_l^1, \theta_l^1, ..., u_l^9, v_l^9, \theta_l^9\}^T \tag{2a}$$

$$\underline{u}_g = \{u_g^1, v_g^1, \theta_g^1, ..., u_g^9, v_g^9, \theta_g^9\}^T \tag{2b}$$

where u^k, v^k, and θ^k denote the displacement of two translations and rotation in the kth nodes. Thus, it is possible to express the virtual work by equating the transformation matrix ($\underline{\underline{B}}$) between the local and global load vectors as follows:

$$V = \delta\underline{u}_g^T \underline{f}_g = \delta\underline{u}_l^T \underline{f}_l \tag{3}$$

$$\delta\underline{u}_g = \underline{\underline{B}}\delta\underline{u}_l \tag{4}$$

where the transformation matrix is obtained by considering the rotational operator ($\underline{\underline{E}}$) and the projector matrix ($\underline{\underline{P}}$) in [17].

Finally, the tangent stiffness matrix and internal load vector in the global coordinates are as follows:

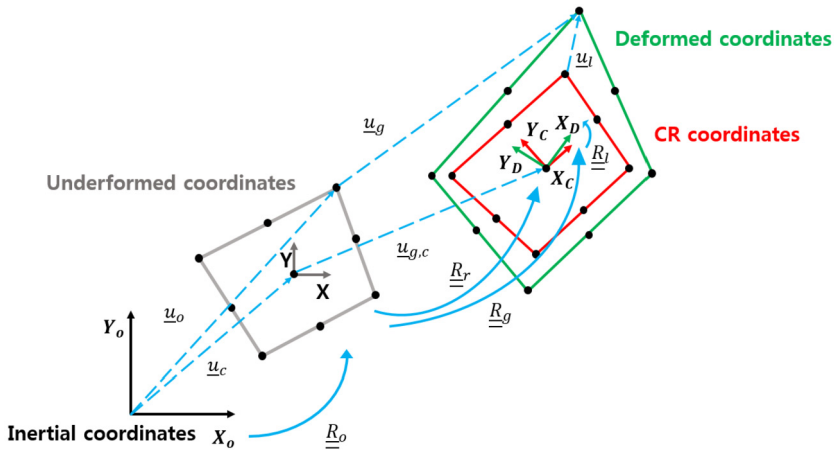

Fig. 2. Descriptions for inertial, undeformed, CR, and deformed coordinates.

$$\underline{\underline{K}}_g = \underline{\underline{B}}^T \underline{\underline{K}}_l \underline{\underline{B}} + \underline{\underline{E}}(-\underline{F}\underline{G}^T - \underline{G}\underline{F}^T \underline{\underline{P}})\underline{\underline{E}}^T \tag{5}$$

$$\underline{f}_g = \underline{\underline{B}}^T \underline{f}_l \tag{6}$$

where the additional vectors, $\underline{F}$ and $\underline{G}$, are described in [17,19].

Similarly, the global mass matrix ($\underline{\underline{M}}_g$) is obtained from the local mass matrix ($\underline{\underline{M}}_l$) as follows:

$$\underline{\underline{M}}_l = \int_\Omega \rho \underline{\underline{N}}_s^T \underline{\underline{N}}_s d\Omega \tag{7}$$

$$\underline{\underline{M}}_g = \underline{\underline{E}}\underline{\underline{M}}_l \underline{\underline{E}}^T \tag{8}$$

where ρ and $\underline{\underline{N}}_s$ denote the density and shape functions of the 9-node planar elements, respectively. Thus, the inertial load vector with respect to the global coordinates is expressed as follows:

$$\underline{f}_g = \underline{\underline{M}}_g \ddot{\underline{u}}_g + \left[\frac{\partial \underline{\underline{M}}_g}{\partial \theta_r} \underline{\underline{G}}\underline{\underline{E}}\dot{\underline{u}}_g\right]\dot{\underline{u}}_g - \left[\frac{1}{2}\dot{\underline{u}}_g^T \left(\frac{\partial \underline{\underline{M}}_g}{\partial \theta_r}\right)\dot{\underline{u}}_g\right]\{\underline{\underline{G}}\underline{\underline{E}}\}^T \tag{9}$$

Based on Lagrange's equation of motion, derivatives of the mass matrix ($\dot{\underline{\underline{M}}}_g$), rigid rotational component (θ_r), and other mathematical forms are well expressed in [19–21].

2.1.2. Material nonlinearity

In reality, an aft closure exhibits elasto-plastic behaviors due to the high pressurized plume loading and its high aspect ratio of thickness and length as shown in Fig. 1. In order to predict elastic/plastic strain components in aft closure, the plane stress-projected plasticity model [22] is extended and used to consider the CR formulation [19]. The present numerical approach is an implicit integration algorithm for the plane stress-projected von Mises model with isotropic hardening. In the procedure, the incremental strain ($\Delta\underline{\epsilon}$) is evaluated by compensating for the discontinuous configurations obtained by CR and deformed coordinates. A localized transformation matrix ($\underline{\underline{F}}$) is defined by using Jacobian matrix relations with respect to each coordinate as follows:

$$\underline{\underline{F}} = \underline{\underline{J}}_C^{-T} \underline{\underline{J}}_D \tag{10}$$

Based on the EICR description, the incremental strain of the 9 node element is evaluated by using the derivatives of shape functions in [23] as follows:

$$\Delta\underline{\epsilon} = \underline{\underline{F}}\underline{\underline{B}}_m^T \underline{\underline{B}}\Delta\underline{u}_g = \underline{\underline{F}}\underline{\underline{B}}_m^T \Delta\underline{u}_l \tag{11}$$

During the elastic predictor state, the trial elastic strain, stress and accumulated plastic strain in the pseudo time are defined as follows:

$$\underline{\epsilon}_{n+1}^{e\text{-}trial} = \underline{\epsilon}_n^e + \Delta\underline{\epsilon} \tag{12a}$$

$$\underline{\sigma}_{n+1}^{trial} = \underline{\underline{D}}^e \underline{\epsilon}_{n+1}^{e\text{-}trial} \tag{12b}$$

$$\underline{\epsilon}_{n+1}^{p\text{-}trial} = \underline{\epsilon}_n^p \tag{12c}$$

where the subscript n and the superscripts e and p indicate the number of incremental elastic state and plastic state, respectively, in the pseudo time ($[t_n, t_{n+1}]$). The trial elastic stress is used to determine plastic admissibility based on the value of the yield function (Φ) obtained by a combination of ($\underline{\underline{P}}$) and ($\underline{\sigma}$).

$$\Phi = \frac{1}{2}\xi^{trial} - \frac{1}{3}\sigma_y^2(\epsilon_{n+1}^{p\text{-}trial}) \tag{13}$$

If the trial elastic strain is admissible ($\Phi^{trial} < 0$), the Newton–Raphson return-mapping algorithm is applied to satisfy the consistency condition as follows:

$$\frac{1}{2}\underline{\sigma}_{n+1}^T \underline{\underline{P}}\sigma_{n+1} - \frac{1}{3}\underline{\sigma}_y^2(\underline{\epsilon}_n^p + \Delta\gamma\sqrt{\frac{2}{3}\underline{\sigma}_{n+1}^T \underline{\underline{P}}\underline{\sigma}_n}) = 0 \tag{14}$$

In the implicit algorithm, the plastic multiplier ($\Delta\gamma$) is initialized and updated in each Newton–Raphson iteration as follows:

$$\Phi' = \frac{1}{2}\xi'(\underline{\sigma}_{n+1}^{trial}, \Delta\gamma) - \frac{1}{3}H'(\xi, \xi', \Delta\gamma) \tag{15a}$$

$$\Delta\gamma = \Delta\gamma - \frac{\Phi}{\Phi'} \tag{15b}$$

The updated yield function is satisfied within tolerance ($|\Phi_n| \leq \epsilon_{tol}$), and the trial elastic stress, plastic strain, and the elasto-plastic consistent tangent matrix ($\underline{\underline{D}}^{ep}$) are newly evaluated as follows:

$$\underline{\sigma}_{n+1} = \underline{\underline{A}}(\Delta\gamma)\underline{\sigma}_{n+1}^{trial} \tag{16a}$$

$$\underline{\epsilon}_{n+1} = [\underline{\underline{D}}^{ep}]^{-1}\underline{\sigma}_{n+1} \tag{16b}$$

$$\underline{\epsilon}_{n+1}^{p\text{-}trial} = \underline{\epsilon}_n^p + \Delta\gamma\sqrt{\frac{2}{3}}\xi(\Delta\gamma) \tag{16c}$$

where, the diagonal matrix $\underline{\underline{A}}(\Delta\gamma)$ and detailed mathematical forms are explicitly given in [22].

Finally, the local stiffness matrix and internal force vector are defined as follows:

$$\underline{\underline{K}}_l = \int_\Omega \underline{\underline{F}}\underline{\underline{B}}_m^T \underline{\underline{D}}^{ep} \underline{\underline{B}}_m \underline{\underline{F}}^T d\Omega + \underline{\underline{K}}_l^s \tag{17}$$

where $\underline{\underline{D}}^{ep}$ denotes the updated elastoplastic consistent tangent matrix that satisfies the consistency condition in Eq. (14). Detailed mathematical formulations for the higher order solid-like membrane element and planar element including the in-plane degrees of freedom are given in [19].

2.1.3. Contact analysis

With respect to a contact between the aft closure and inclined GGT shown in Fig. 1, the Lagrange multiplier approach is used to evaluate the reaction force by multiplying the gap distance and Lagrange multiplier. The variation in the contact constraint is as follows:

$$\delta\Pi_c = \delta\underline{\lambda}^T \underline{g} + (\delta\underline{u}^s - \delta\underline{u}^m)^T \underline{\lambda} \tag{18}$$

where $\underline{\lambda}$ denotes Lagrange multipliers, and $\underline{u}^s$ and $\underline{u}^m$ denote penetration between the slave and master body. The system of the contact condition is expressed in a linearized tangent matrix term as follows:

$$\underline{\underline{K}}_c d\underline{u}_c = \begin{bmatrix} 0 & 1 & 0 \\ 1 & 0 & -1 \\ 0 & -1 & 0 \end{bmatrix} \begin{Bmatrix} d\underline{u}^s \\ d\lambda \\ d\underline{u}^m \end{Bmatrix} = \begin{Bmatrix} -\lambda \\ -g \\ \lambda \end{Bmatrix} = \underline{f}_c \tag{19}$$

2.1.4. Transient analysis based on Newmark-β method

Various numerical integration methods were explored for structural dynamics. However, in the present study, Hilber–Hughes–Taylor (HHT-α) method is adopted for the transient analysis. Specifically, HHT-α is generally used in structural dynamics for the numerical integration of second order accuracy. In the method, two steps are applied, namely the predictor step to assume an exact satisfaction of the dynamic equilibrium and the corrector step to satisfy the equilibrium state between the internal and external forces. The governing equation of HHT-α method is briefly defined as follows:

$$\begin{aligned} &\underline{\underline{M}}\ddot{\underline{u}}^{n+1} + (1-\alpha)\underline{\underline{C}}\dot{\underline{u}}^{n+1} + \alpha\underline{\underline{C}}\dot{\underline{u}}^{n} + (1-\alpha)\underline{\underline{K}}\underline{u}^{n+1} + \alpha\underline{\underline{K}}\underline{u}^{t} \\ &\quad = (1-\alpha)\underline{f}_{ext}^{n+1} + \alpha\underline{f}_{ext}^{n} \end{aligned} \tag{20}$$

where the $\underline{\underline{C}}$, $\underline{f}_{ext}$ and the superscript n denote the damping matrix, external force vector, and an index of the time step, respectively. In each time step, the displacements, velocities, and accelerations are updated as follows:

$$\underline{u}^{n+1} = \underline{u}^n + \delta\underline{u}^n \tag{21}$$

$$\ddot{\underline{u}}^{n+1} = (\frac{1}{\beta h})^2(\underline{u}^{n+1} - \underline{u}^n) - (\frac{1}{\beta h})(\dot{\underline{u}}^{n+1}) \tag{22}$$

$$\dot{\underline{u}}^{n+1} = \dot{\underline{u}}^n + h((1-\gamma)\ddot{\underline{u}}^n + \gamma\ddot{\underline{u}}^{n+1}) \tag{23}$$

The remaining α, β, and γ are constants in the HHT-α method in [24].

2.2. Governing equation for fluid analysis

2.2.1. Compressible computational fluid dynamics

Two-dimensional Eulerian equations are analyzed to simulate highly pressurized plume ignited from the rocket in the VLS. The equation of the state in the fluid is treated as an ideal gas. The corresponding governing equations are solved by the third-order Runge–Kutta method and the convex essentially non-oscillatory (CENO) method in spatial and temporal discretizations, respectively [25].

$$\frac{\partial\rho}{\partial x} + \frac{\partial}{\partial x}(\rho u_x) + \frac{\partial}{\partial y}(\rho u_y) = 0 \tag{24}$$

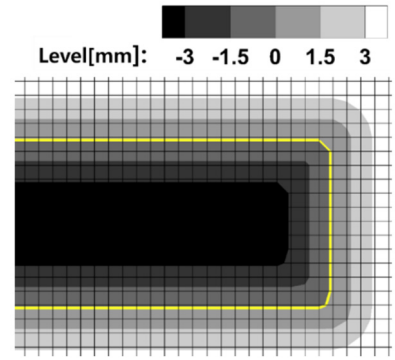

Fig. 3. Interface modeling between the fluid and structure based on the level-set method.

$$\frac{\partial}{\partial t}(\rho u_x) + \frac{\partial}{\partial x}(\rho u_x^2 + P) + \frac{\partial}{\partial y}(\rho u_x u_y) = 0 \tag{25}$$

$$\frac{\partial}{\partial t}(\rho u_y) + \frac{\partial}{\partial x}(\rho u_x u_y) + \frac{\partial}{\partial y}(\rho u_x^2 + P) = 0 \tag{26}$$

$$\frac{\partial}{\partial t}(\rho e) + \frac{\partial}{\partial x}[u_x(\rho e + P)] + \frac{\partial}{\partial y}\left[u_y(\rho e + P)\right] = 0 \tag{27}$$

$$P = \rho RT \tag{28}$$

ρ, u_x, u_y, P, e, R and T denote the density, velocity in the x-direction, velocity in the y-direction, pressure, total energy, gas constant and temperature, respectively in the above equations. The inlet boundary condition located in nozzle exit is defined by using the rocket plume parameters obtained from NASA CEA code based on the AP mole fraction [26]. The detailed parameters are described in the following section.

2.3. Tightly coupled fluid–structure interaction

2.3.1. Hybrid level-set method

Based on the level-set method, it is possible to track the interface (boundary) between the gaseous mixture and structures in the Eulerian coordinates. A zero value of level-set ($\phi = 0$) indicates the interface of multi-materials. If the value of the level becomes positive ($\phi > 0$), it corresponds to the inner region of the solid structure. Along the interface, ghost fluid method (GFM) is utilized to address the discontinuous properties [25]. The properties of the ghost nodes, such as pressure and density, are obtained by using extrapolation process. The boundary between the fluid and structure is determined by using Jordan curve theorem in [27]. Further details are described in [28].

In Fig. 3, the boundary between the fluid and structure is described by a yellow line by using seven different levels. Although more accurate conditions are obtained by increasing the number of levels, it requires increased computational time. In the study, nine levels are applied to track the interface.

2.3.2. Algorithm for tightly coupled two-way FSI

A two-way tight coupling approach is established to couple the structural with the compressible dynamic analysis. A one-way explicit coupling approach is developed in an extant study [28]. However, in the present FSI analysis, the pressure and deformed configuration as obtained by each fluid/structural analysis are exchanged at each time step through the interface level. The explicit algorithm is briefly described in Fig. 4.

Fig. 5 shows the simplified configuration for a clamped boundary at its root in the structural analysis. When the fluid analysis estimates the pressure distribution along the interface level, the force vector is obtained based on the x and y directions at each structural node. Fig. 5a shows the deformed configuration in the

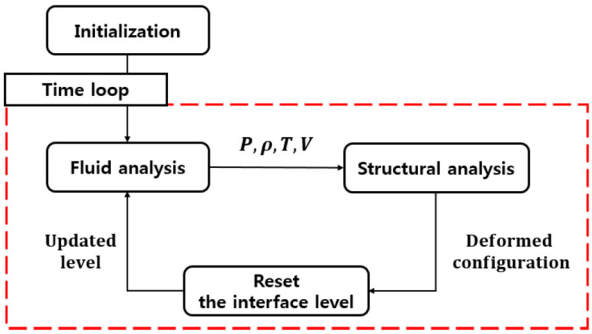

Fig. 4. Algorithm of the present two-way coupling approach.

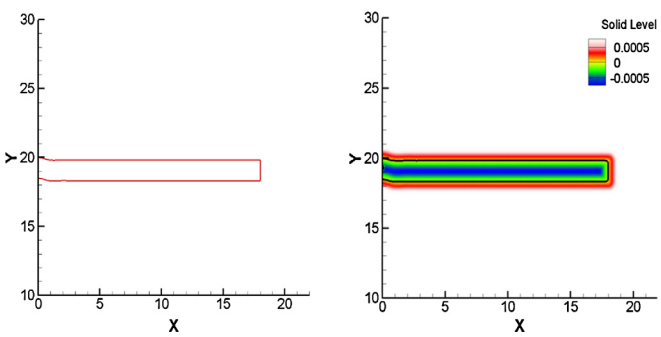

(a) Deformed configuration in the structural analysis (b) Replaced configuration in the fluid analysis

Fig. 5. Deformed configuration in each analysis.

structural coordinates. Given the estimated values of ghost nodes, the interface level is replaced into the fluid analysis as shown in Fig. 5b.

Finally, a simplified configuration of the VLS is conducted. Fig. 6 shows the three deformed configurations in the opening procedure. Although one of the aforementioned approaches, i.e., the arbitrary Lagrangian–Eulerian (ALE) method, was suggested for nonlinear problems of geomechanics, only limited studies explore the same including solid-rigid contact [29]. However, the novelty of the approach is that it involves geometrical/material nonlinear behaviors of structure including the contact mechanism. Although a severely torted mesh must be carefully treated along the interface between the fluid and structures [30], the present approach does not require the regeneration of the mesh in the region of contacted/reflected side.

3. Validation

In this section, numerical results are compared with those obtained in the commercial programs (ANSYS and ABAQUS) to verify the present fluid and structural analysis. Additionally, the present tightly coupled two-way FSI analysis is also validated with the results obtained by ANSYS FSI. All the numerical validations are obtained by use of the two-dimensional solutions.

3.1. Compressible CFD

First, the present fluid analysis is examined by comparing it with the pressure distribution obtained by ANSYS FLUENT. Inviscid model is used to validate present numerical results. Fig. 7 shows the idealized configuration of the VLS in which the rocket plume (red colored area) is propagated, reflected by the bottom wall (black colored area), and finally exhausted into the outlet (blue colored area). Hot exhaust gas is assumed as an ideal gas at a speed of 1,200 m/s, at a temperature of 2,500 K, and under ambient atmospheric pressure at the inlet. The outflow (zero-gradient) condition is used to discharge the internal flow. The grid size for present analysis and ANSYS FLUENT is fixed with 0.001 m.

Fig. 8 shows the pressure history predicted at the measured location and the pressure distribution. Thus, the present examination indicates a good correlation in terms of pressure relative to those obtained by ANSYS FLUENT. Further validations are suggested by the present authors in [28].

3.2. Geometrical/material nonlinearity

In the example, a cantilevered beam under the tip load is examined to compare the displacement history between elastic and elasto-plastic analyses. Elastic and elasto-plastic analyses are conducted by using the material properties in Table 1. The tip displacement history in the elastic analysis indicates the oscillatory behavior of the restored energy. However, the oscillatory behavior is estimated after the larger displacement is obtained in the elasto-plastic analysis. Both results suggest an error of less than 1% when compared with those obtained by ABAQUS.

3.3. Contact mechanism

A cantilevered beam with two rigid walls under the uniform pressure should be analyzed to consider the reflection from the inclined angle of the plenum. In a manner to that shown in Fig. 9, elastic/plastic analyses are conducted. The elastic analysis indicates that the tip displacement history reveals two reflecting behaviors from the lower and upper rigid walls. Conversely, a plastic behavior

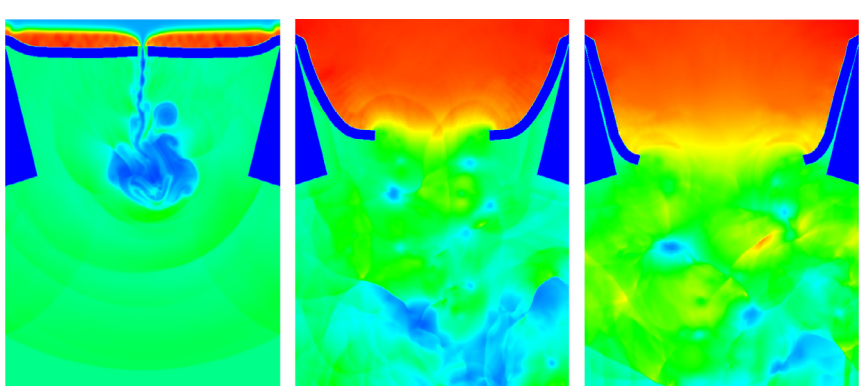

(a) Opening sequence 1 (b) Opening sequence 2 (c) Opening sequence 3

Fig. 6. Opening sequences in the simplified VLS.

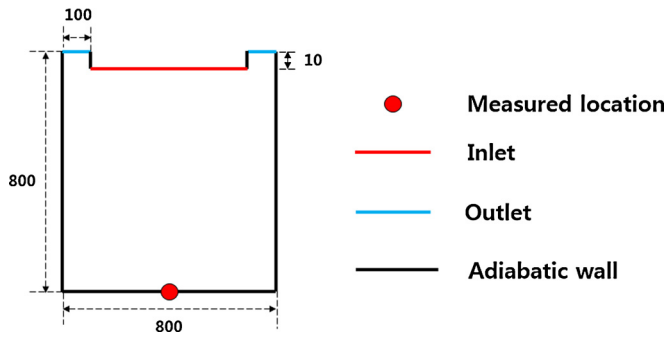

Fig. 7. Idealized configuration of a canister.

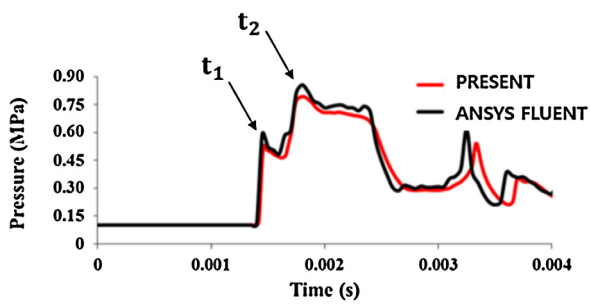

(a) Comparison of the pressure history at the measured point

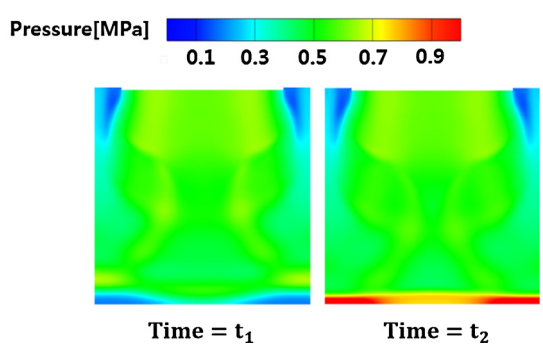

(b) Pressure distribution at time t_1 and t_2

Fig. 8. Numerical results of the fluid analysis.

Table 1
Material properties used in the elastic and elasto-plastic analyses.

	Value
Young's modulus (GPa)	210
Poisson's ratio	0.3
Yield stress (GPa)	0.248
Hardening coefficient (GPa)	50
Material density (kg/m^3)	7800
Length (m)	10
Height and thickness (m)	10

Table 2
Material properties used in the present contact analysis.

	Value
Young's modulus (GPa)	210
Poisson's ratio	0.3
Yield stress (GPa)	0.248
Hardening coefficient (GPa)	50
Density (kg/m^3)	7800
Length and thickness (m)	1
Height (m)	0.02
Pressure (MPa)	1

in the cantilevered beam is reflected and sticks to the wall. The present results are further validated by the using various types of finite elements in Ref. [19]. See Table 2 and Fig. 10.

3.4. Two-way FSI analysis

Finally, a simple flow configuration is used to validate the present tightly coupled FSI analysis since the experimental results for the VLS are unavailable. In the present FSI analysis, a cantilevered structure is deflected by high-speed aerodynamic loads to a maximum speed of 200 m/s in Fig. 11a. Arbitrary material properties are introduced to exaggerate tip displacement at the measured location with respect to the flow conditions. The horizontal displacement history at the measured location is comparatively consistent with that obtained by ANSYS FSI. Table 3 summarizes the parameters of the present fluid, structural, and FSI analyses. The detailed results are shown in Ref. [28].

4. Results of the parametric analysis

In the section, numerical results of the parametric study are presented. The present analysis uses a configuration that is similar

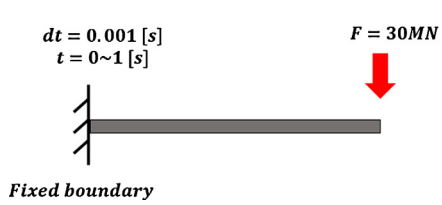

(a) Cantilevered beam under the tip load

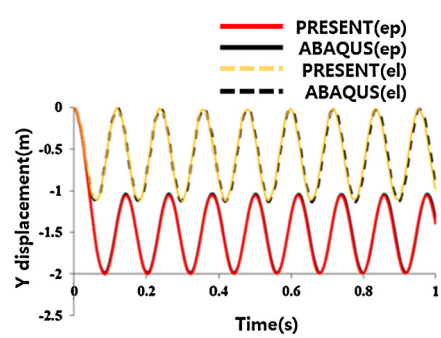

(b) Tip displacement history between the elastic(el) and elasto-plastic(ep) analyses

Fig. 9. Numerical results of the structural analysis.

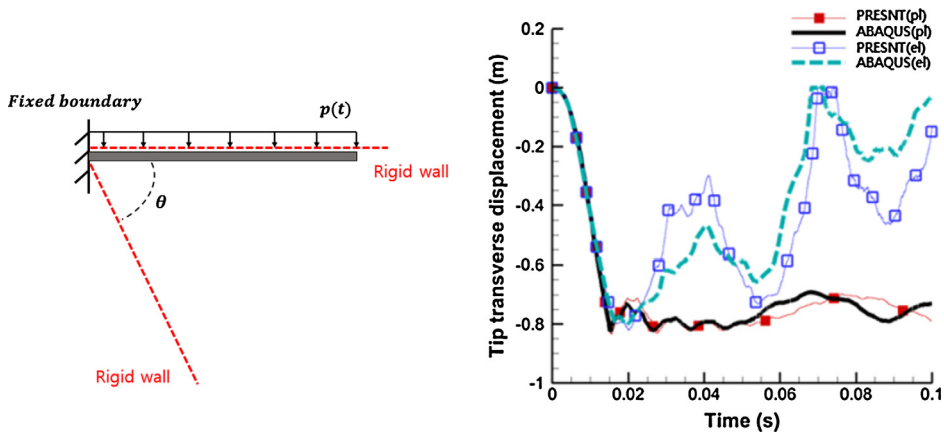

(a) Cantilevered beam under uniform pressure

(b) Tip displacement history between the elastic/plastic analysis

Fig. 10. Numerical results for the contact mechanism.

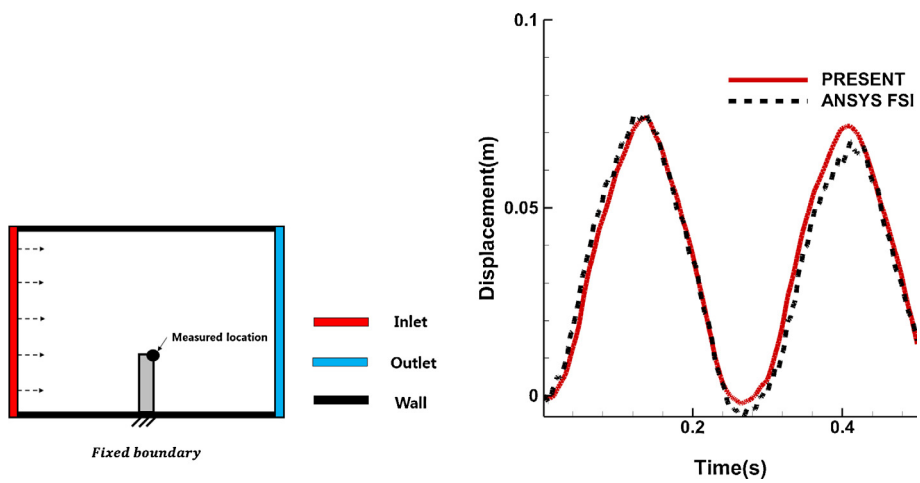

(a) Simple flow configuration of the FSI analysis

(b) Comparison of the hor izontal displacement at the measured location

Fig. 11. Numerical results of the present FSI analysis.

Table 3
Parameters of the present fluid, structural and FSI analyses.

Analysis type	Parameter	Value
Fluid analysis	Density (kg/m^3)	1.225
	Mesh size (m)	0.05
Structural analysis	Density (kg/m^3)	7850
	Young's modulus (MPa)	20
	Poisson's ratio	0.3
	Mesh size (m)	0.05
FSI analysis	Timestep (s)	0.001
	Number of steps	500
	Total time (s)	0.5

to that of MK-41 [31]. Specifically, T and D indicate the thickness of the aft-closure and angle of the inclined plenum, respectively. For example, $T10$–$D75$ denotes the configuration of the VLS at a thickness of 10 mm corresponding to the aft-closure and 75° of the inclined plenum. Before conducting the parametric analysis, three different grid sizes, 1 mm, 2 mm, and 5 mm, are tested for accuracy of present FSI analysis. As a result, the necessary grid size is determined to be 2 mm. First, an initial configuration of the VLS ($T10$–$D75$) is examined to understand the interaction between the complex flow field and opening/closing aft-closure. Subsequently, twenty-one cases of the parametric studies are further examined while varying the range of aft-closure thickness from 8 mm to 10 mm and the angle of the inclined plenum from 45° to 75° at an interval of 1 mm and 5°.

4.1. Two-way FSI analysis for the VLS

Fig. 12a shows the deflected aft-closure by the rocket plume after the adjacent missile is launched. The deflected aft-closure on the left canister does not return to the original configuration due to the plastic effect. In order to predict the situation, time-varying pressure obtained in Fig. 8 is applied in the present aft-closure. Finally, the deflected configuration of the aft-closure on the adjacent canister is used in Fig. 12b.

The parameters used in the present FSI analysis are listed in Table 4. The details of the rocket plume composition AP/HTPB propellant are given in Ref. [28]. Three instrumentation locations (A, B, and C) are used to predict the magnitude of the pressure, temperature, and mass flow rate. The lines correspond to one of the factors to extract an efficient configuration of the VLS. In the preliminary design for VLS, temperature applied to the bottom plenum should be reduced to avoid the ablation phenomenon. Additionally, the

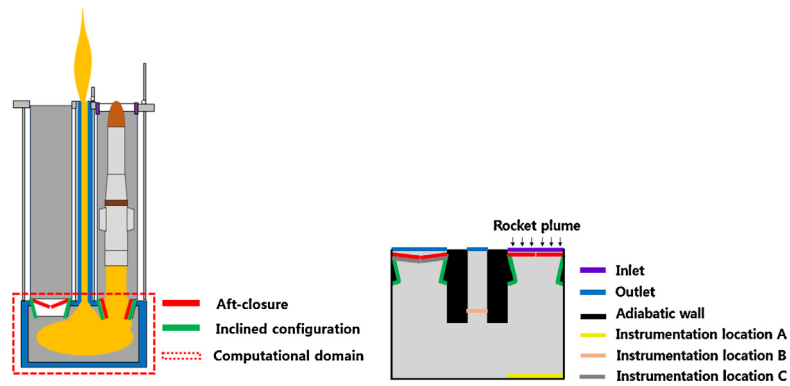

(a) Schematic diagram of the two-canisters in the VLS

(b) Computational domain for the present FSI analysis

Fig. 12. Numerical results of the present FSI analysis.

Table 4
Parameters used in the present FSI analysis.

Analysis	Parameter	Value
Fluid analysis	Specific heat ratio, γ	1.245
	Gas constant, R (J/kg · K)	382.7
	Stagnation pressure, p_0 (bar)	76.86
	Stagnation temperature, T_0 (K)	2155
Structural analysis	Density (kg/m^3)	8000
	Young's modulus (GPa)	200
	Poisson's ratio	0.3
	Yield stress (GPa)	0.215
	Hardening coefficient (GPa)	1
FSI analysis	Time step (s)	1×10^{-7}
	Number of the steps	235000
	Total time (s)	0.0235

amount of the exhaust gas should be ventilated by the central uptake between the two adjacent canisters. It is also necessary for the aft-closure to be completely closed to protect the interiors in the adjacent canister. The detailed comparison of the parametric studies are described in the following section.

Fig. 13 shows the distribution of the pressure and temperature in the sequences. First, a highly compressed rocket plume is ignited from the inlet as shown in Fig. 13a. The aft-closure is deflected by dynamic pressure at 0.55 MPa in Fig. 13b. During the opening event, the aft-closure is not affected by the high temperature. In Fig. 13c, the high pressure is rapidly propagated while the high temperature plume gradually spreads into the bottom of the VLS. It is observed that the aft-closure on the left canister is activated by the acoustic pressure. Finally, the left-hand side aft-closure is completely closed such that the complex flow does not directly impact the left canister as shown in Fig. 13d.

Fig. 14 shows the history of the relevant quantities for $T10D75$. During the opening/closing event, the aft-closure in the adjacent canister is completely closed by the amount of pressure loads at 0.4 MPa as shown in Fig. 14c. The exhaust gas is ventilated within 0.015 to 0.02 s. The average temperature applied to the bottom plenum does not exceed 600 K. It is revealed that the initial configuration of the VLS ($T10D75$) operates as intended for the given condition.

4.2. Parametric studies in terms of the thickness and inclined angle

Finally, 21 cases of the parametric studies are conducted for the preliminary design of the present VLS. Here, the tendency of the flow field propagated in the VLS is also examined. Additionally, the pressure, temperature, and mass flow rate are compared at each line defined in Fig. 12b. Fig. 15. shows three configurations of the VLS. The initial configuration in Fig. 15a is considered as a reference. The red and yellow areas indicate the inclined angle (D) and thickness of the aft-closure (T). The inclined angle varies from D75 (75°) to D45 (45°) in Figs. 15a and 15b. Thus, the thickness of the aft-closure changes from T10 (10 mm) to T08 (8 mm). Specifically in Figs. 15a and 15c, two different configurations of the aft-closure on the left canister are adopted. The aft-closure thickness is varied, and thus the final configuration also shifts.

The history of the temperature distribution for the three cases is shown in Fig. 16. It is observed that the aft-closure contacts the inclined plenum at 0.015 (s) and does not bound off due to the dynamic load. During the opening event, the aft-closure is deflected by the highly compressed rocket plume in the three cases. The relatively low pressure rocket plume exhausts relative with respect to the inclined angle of the plenum are shown in Fig. 16. Additionally, the history of the temperature in the bottom wall is depicted in Fig. 17. This suggests that the inclined angle of the plenum can enhance/alleviate the compressed rocket plume.

Conversely, it is observed that the magnitudes of temperature exhibit an increasing trend with respect to the thickness of the aft-closure, as shown in Fig. 17. This implies that the thickness of the aft-closure may affect the temperature distribution on the bottom wall. Fig. 18 shows the history of the temperature distribution for the following three cases. When the aft-closure thickness increases, the high temperature flow is applied into the bottom wall as shown in Fig. 19. This reveals that the aft-closure plays a significant role in propagating a complex flow field into the plenum. Prior to when the major rocket plume passes by the inclined plenum, a small amount of flow interacts with the aft-closure that is opened. This is due to the difference in the opening configurations of the aft-closure. Additionally, the corresponding shadowgraph contours are shown in Fig. 20. The complex flow field and reflected acoustic waves are developed in the plenum. Acoustic waves are propagated with the reflection of both aft-closure and plenum. Therefore, it is important to consider the interaction between the fluid and structures in the preliminary design of the VLS.

Additionally, the pressure and the mass flow rate are shown in Fig. 21 and Table 5. The average mass flow rate is predicted for the present analysis. Although numerical results do not indicate any significance in terms of the pressure, an interesting aspect relates to the mass flow rate. With respect to the inclined angle of the plenum between 60° and 70°, the maximum exhaust gas is ventilated into the central uptake. In the future, the present analysis

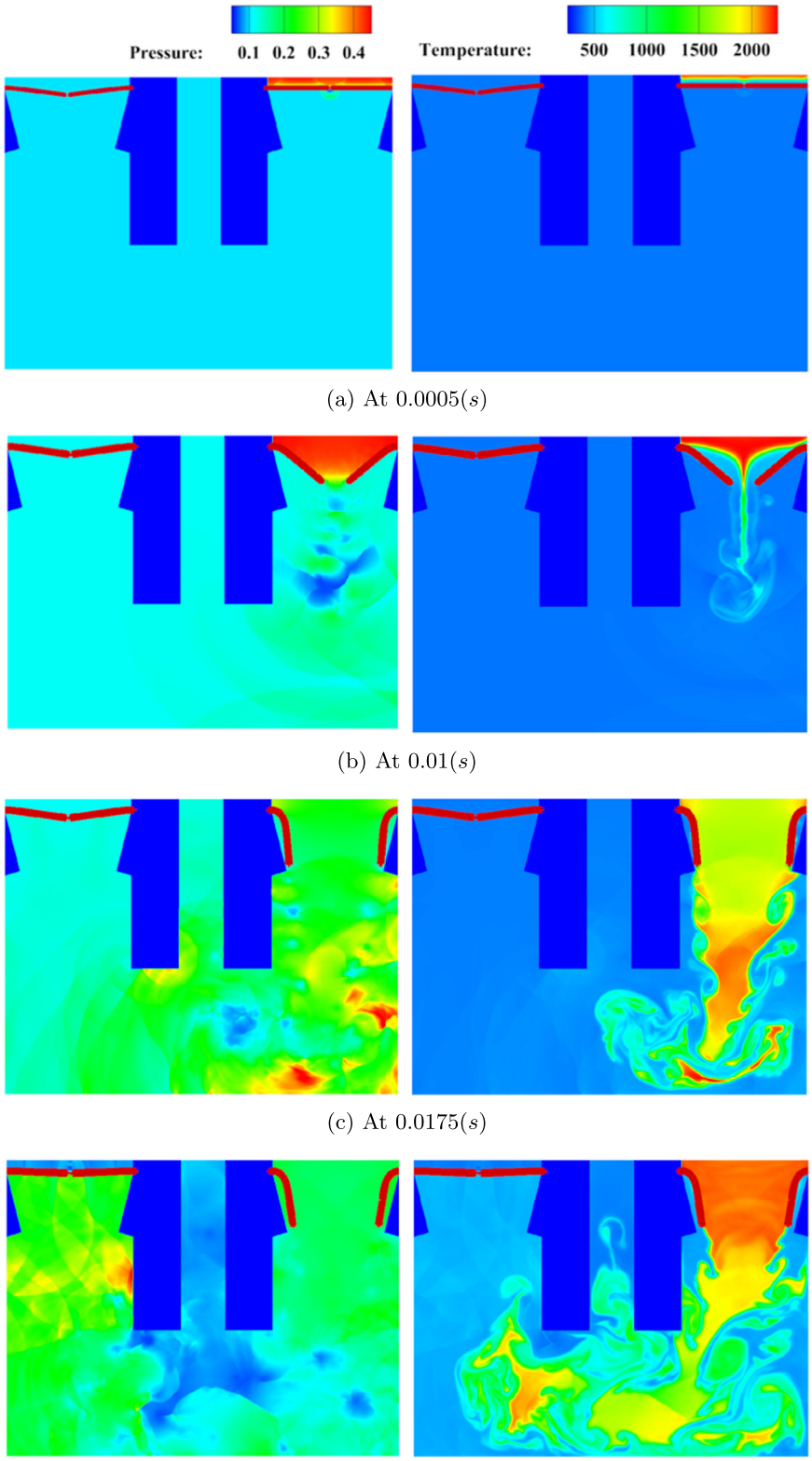

(a) At 0.0005(s)

(b) At 0.01(s)

(c) At 0.0175(s)

(d) At 0.0235(s)

Fig. 13. Snapshots of the pressure and temperature distributions [unit: MPa, K].

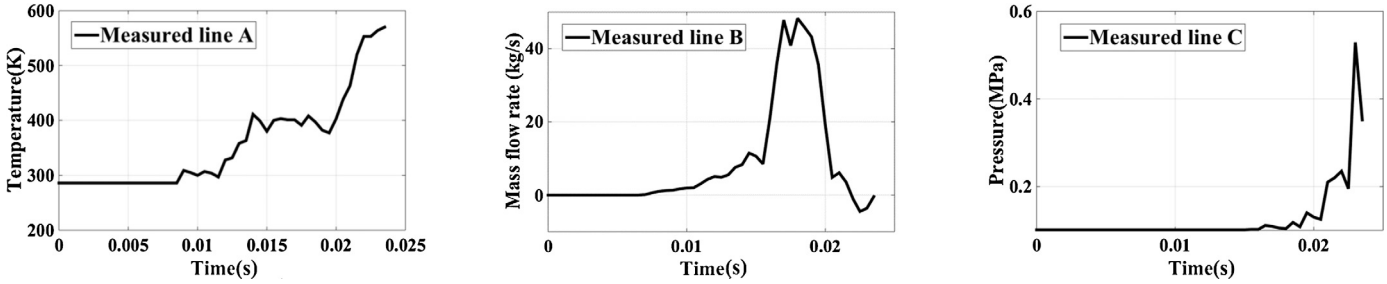

(a) Temperature history at line A (b) Mass flow rate history at line B (c) Pressure history at line C

Fig. 14. Numerical results for the $T10$–$D75$.

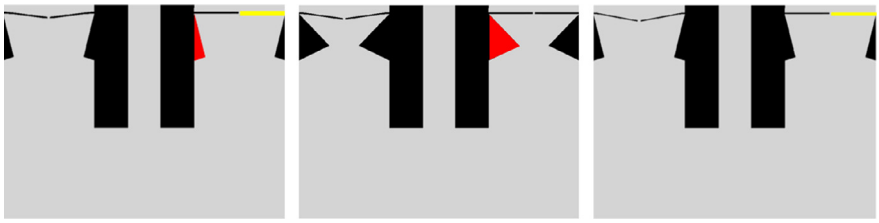

(a) Initial configuration (b) Inclined angle variation (c) Thickness of the aft-closure variation

Fig. 15. Three configurations of the VLS in terms of T and D parameters.

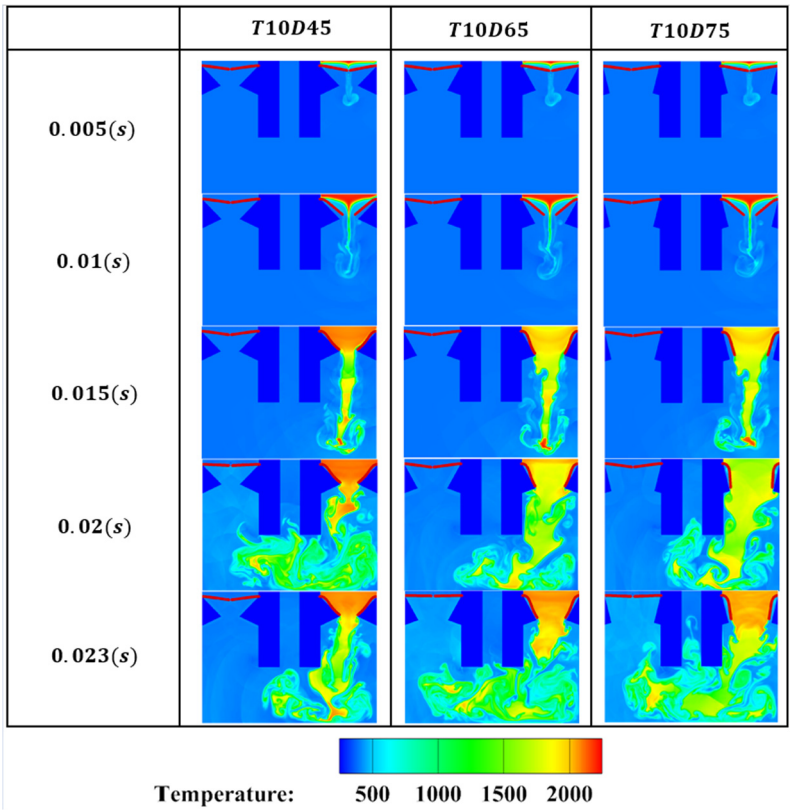

Fig. 16. Temperature distribution for the $T10D45$, $T10D65$, $T10D75$.

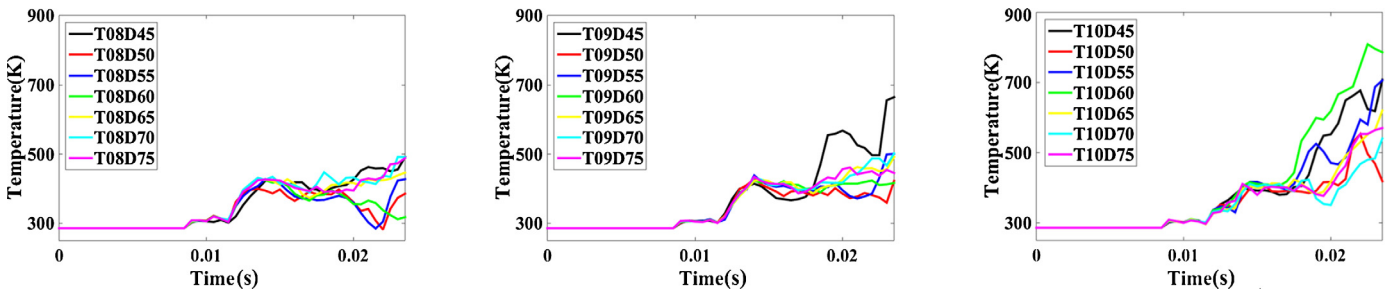

(a) $T08$ cases (b) $T09$ cases (c) $T10$ cases

Fig. 17. Temperature history obtained at the bottom wall.

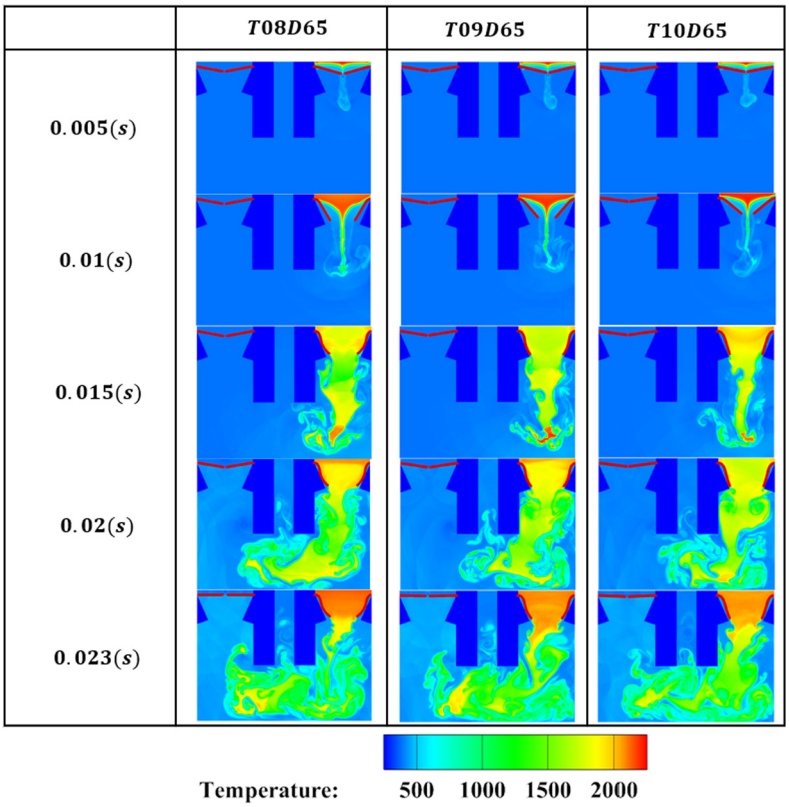

Fig. 18. Temperature distribution for the $T08D65$, $T09D65$, $T10D65$.

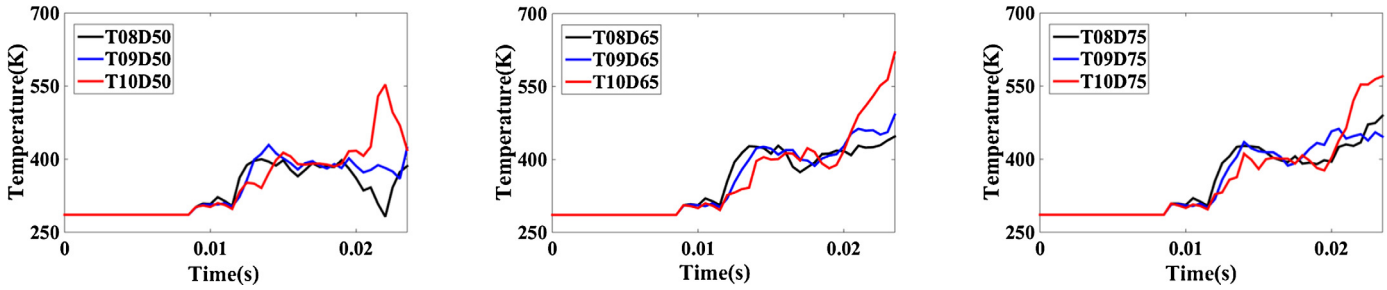

(a) $D55$ cases (b) $D65$ cases (c) $D75$ cases

Fig. 19. Temperature history obtained from the bottom wall.

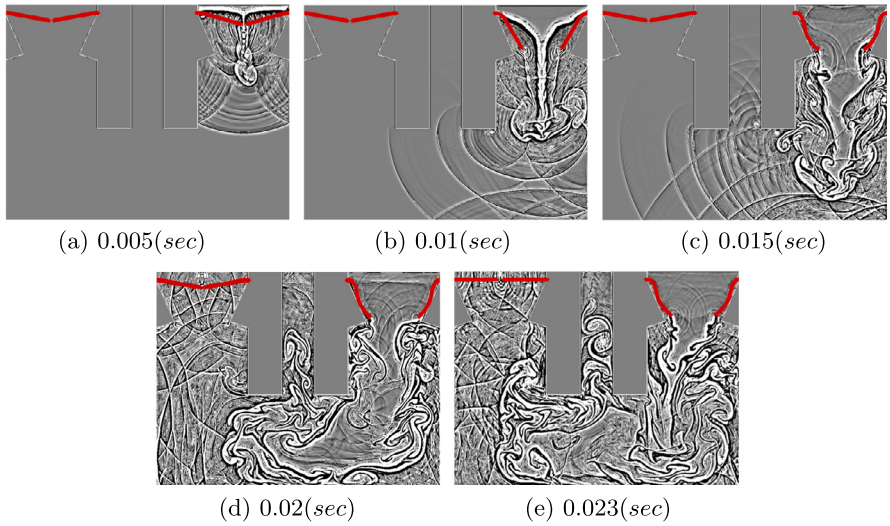

Fig. 20. Shadowgraph contours for the $T08D65$ case.

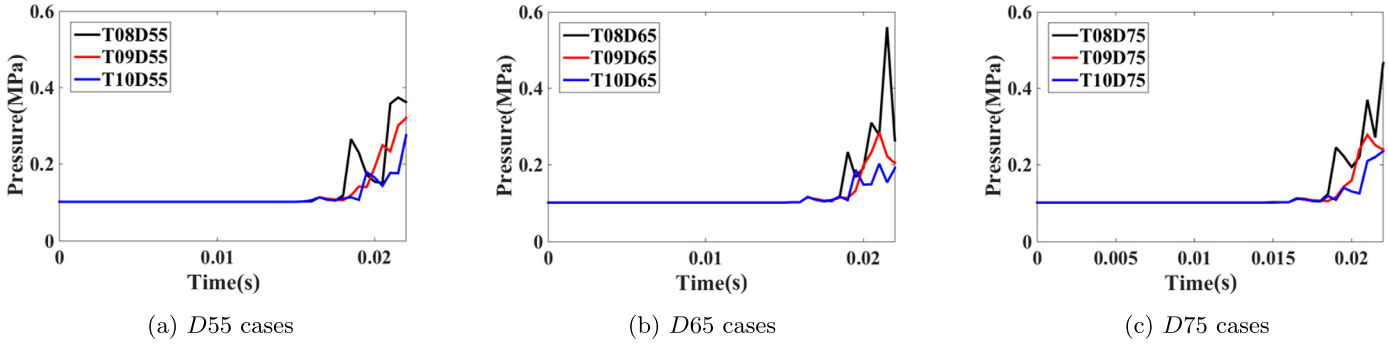

Fig. 21. History of pressure obtained from the adjacent aft-closure.

Table 5
Average of the mass flow rate (kg/s).

	T08	T09	T10
D45	8.53	9.08	9.62
D50	8.44	9.84	9.51
D55	9.79	9.63	8.98
D60	9.96	9.62	**10.42**
D65	9.66	10.15	9.86
D70	**11.10**	**10.15**	8.84
D75	10.47	9.06	9.05

will be extended to investigate the primary concerns of VLS design by considering additional parameters. Extant studies reported that plate shocks at the bottom plenum exhibited an almost a linear decrease relative to the distance away from the nozzle exit as indicated in Ref. [15]. Additionally, the mass flow rate of exhaust gas increases when a conical deflector is adopted at the bottom wall in Ref. [32]. Therefore, a variety of parameters are used including the height and width of the plenum, the gap between two canisters.

Two factors, namely the aft-closure thickness and inclined angle of the plenum, are varied to design an efficient VLS. Based on the reference configuration of the VLS shown in Fig. 12b, a comparatively lower temperature distribution is obtained by applying a thinner aft-closure at the bottom wall. This is because the interaction between the rocket plume and deforming aft-closure can affect the pressure propagation in the opening event. Subsequently, the complex flow field spreads into the VLS with reflecting acoustic waves. Additionally, the variation in the inclination angle is potentially beneficial in alleviating the compressed rocket plume induced by the presence of the aft-closure. The present parametric studies outline the adoption of a thinner aft-closure with an increased inclination angle for the plenum to ventilate the exhaust gas into the central uptake.

5. Conclusion

The study proposes a tightly coupled two-way FSI simulation for a VLS. The CR formulation is used to estimate large deflection in the aft-closure and is extended to predict the elasto-plastic behaviors of the aft-closure. A contact mechanism is also included to describe the deflection bounced from the inclined plenum. Eulerian equations are analyzed to describe AP based rocket plume. In the FSI simulation, the pressure and deflection along the interface are exchanged by using ghost nodes based on the level-set method. The present numerical results indicate good correlation with the results obtained by using ABAQUS and ANSYS. Finally, the present FSI analysis for the VLS is conducted for the operations in which the adjacent aft-closure is fully closed by the propagated acoustic loads. Furthermore, two key factors are investigated for the preliminary design of the VLS. Given the opening motions of the aft-closure, the interaction between the structural and fluid flow should be considered to predict the complex flow field. The parametric studies suggest that a thinner aft-closure of the VLS induces an alleviation in the temperature applied to the bottom wall of the plenum. When the inclination angle is not sufficiently high for the flow to pass into the plenum, the compressible rocket plume stagnates due to the presence of the aft-closure and the plenum. In the future, the present analysis will be extended to consider additional parameters such as the height and width of the plenum and the gap between the two canisters.

Conflict of interest statement

The researchers claim no conflicts of interest.

Acknowledgements

This work was conducted at High-Speed Vehicle Research Center of KAIST with the support of the Defense Acquisition Program Administration and the Agency for Defense Development under Contract UD170018CD.

References

[1] J.H. Gummer, B.L. Hunt, The impingement of a uniform, axisymmetric, supersonic jet on a perpendicular flat plate, Aeronaut. Q. 22 (4) (1971) 403–420.
[2] C.V. Knight, Experimental investigation of two-dimensional, supersonic flow impingement on a normal surface, AIAA J. 11 (2) (1973) 233–235.
[3] P.J. Lamont, B.L. Hunt, The impingement of underexpanded axisymmetric jets on wedges, J. Fluid Mech. 76 (1976) 307–336.
[4] K.Y. Chien, T.F. Zien, R.T. Drifymyer, Two-dimensional supersonic jet impingement on a flat plate, AIAA J. 17 (1979) 4–5.
[5] A.M. Al-Qutub, M.O. Budair, Experiments on the flow over a flat surface impinged by a supersonic jet, in: Proceeding of the 31st Joint Propulsion Conference and Exhibit, San Diego, CA, 1995, paper AIAA-95-2395.
[6] W. Masuda, E. Moriyama, Aerodynamic characteristics of underexpanded coaxial impinging jets, JSME Int. J. Ser. B 37 (1994) 769–775.
[7] F.S. Alvi, K.G. Iyer, Mean and unsteady flowfield properties of supersonic impinging jets with lift plates, in: Proceeding of the 5th AIAA/CEAS Aeroacoustics Conference and Exhibit, Bellevue, WA, 1999, paper AIAA-99-1829.
[8] A. Rubel, Inviscid axisymmetric jet impingement with recirculating stagnation regions, AIAA J. 21 (3) (1983) 351–357.
[9] K.H. Kim, K.S. Chang, Three-dimensional structure of a supersonic jet impinging on an inclined plate, J. Spacecr. Rockets 31 (5) (1994) 778–782.
[10] J.J. Yagla, Internal ballistics of weapon launching systems, Nav. Eng. J. (1983) 178–191.
[11] J.J. Bertin, R.S. Bertin, A. Yung, The launch-tube flow-field for a vertical launching system, in: Proceeding of the AIAA 26th Aerospace Sciences Meeting, Reno, Nevada, 2003, paper AIAA-88-0332.
[12] S.K. Hong, K.S. Lee, D.K. Back, Simulation of jet plume impinging onto a duct, J. Comput. Fluids Eng. 2 (2) (1997) 44–50.
[13] K.S. Lee, S.K. Hong, S.O. Park, Internal flow characteristics of vls type canister, in: Proceedings of the First National Congress on Fluids Engineering, Korean Society of Mechanical Engineerings, 2000, pp. 511–514.
[14] K.S. Lee, S.K. Hong, S.O. Park, Improvement in flux-difference splitting algorithm for accurate and robust flow simulation, Comput. Fluid Dyn. J. 10 (2) (2001) 181–191.
[15] K.S. Lee, S.K. Hong, S.O. Park, Supersonic jet impingement Navier–Stokes computations for vertical launching system design applications, J. Spacecr. Rockets 41 (5) (2004) 735–744.
[16] C. Rankin, A. Brogan, An element-independent corotational procedure for the treatment of large rotations, J. Press. Vessel Technol. 108 (2) (1989) 165–175.
[17] J.M. Battini, A non-linear corotational 4-node plane element, Mech. Res. Commun. 35 (6) (2008) 408–413.
[18] H. Cho, J.-Y. Kwak, S.-J. Shin, N.-H. Lee, S. Lee, Flapping wing fluid–structural interaction analysis using co-rotational triangular planar structural element, AIAA J. 54 (8) (2016) 2265–2276.
[19] H. Cho, H.S. Joo, S.J. Shin, H. Kim, Elastoplastic and contact analysis based on consistent dynamic formulation of co-rotational planar elements, Int. J. Solids Struct. 121 (2017) 103–116.
[20] H. Cho, S.J. Shin, J.J. Yoh, Geometrically nonlinear quadratic solid/solid-shell element based on consistent corotational approach for structural analysis under prescribed motion, Int. J. Numer. Methods Eng. 112 (5) (2017) 434–458.
[21] H. Cho, H.D. Kim, S.J. Shin, Geometrically nonlinear dynamic formulation for three-dimensional co-rotational solid elements, Comput. Methods Appl. Mech. Eng. 328 (1) (2017) 301–320.
[22] E. Neto, D. Peric, D. Owen, Computational Methods for Plasticity: Theory and Applications, John Wiley & Sons, United Kingdom, 2008.
[23] C.A. Felippa, Introduction to Finite Element Methods, University Lecture, 2012.
[24] M. Crisfield, Non-Linear Finite Element Analysis of Solids and Structures, Advanced Topics, vol. 2, Wiley, Chichester, 1997.
[25] K. Kim, M. Gwak, J. Yoh, An enhanced particle reseeding algorithm for the hybrid particle level set method in compressible flows, J. Sci. Comput. 1 (2014) 1–23.
[26] W. Cai, P. Thakre, V. Yang, A model of ap/htpb composite propellant combustion in rocket-motor environments, Combust. Sci. Technol. 180 (2008) 2143–2169.
[27] J.P. Moreno, An invitation to plane topology, Australian Mathematical Society Gazette 29 (3) (2002) 149–154.
[28] Y. Lee, M. Gwak, H. Cho, H.S. Joo, S.-J. Shin, J. Yoh, Numerical simulation of severely transient fluid structure interaction problem associated with a vertical launching system, J. Spacecr. Rockets 5 (4) (2018) 948–958.
[29] R. Loon, P. Anderson, F.N. Vosse, A fluid–structure interaction method with solid-rigid contact for heart valve dynamics, J. Comput. Phys. 217 (2006) 806–823.
[30] M. Souli, A. Ouahsine, L. Lewin, Ale formulation for fluid–structure interaction problems, Comput. Methods Appl. Mech. Eng. 190 (2000) 659–675.
[31] M. Zimmerman, Mk 41 vertical launching system, Approved for public release.
[32] S. Saha, D. Chakraborty, Plume-ducting system design of vertical launcher using computational-fluid-dynamics tools, J. Spacecr. Rockets 50 (3) (2013) 715–718.